

Chiral Spin Textures Driven by Emergent Spin-Orbit Interaction: A Numerical Study

Shuai Yang,¹ Zhiyu Dong,^{2,3} and Yan Chen^{1,4,*}

¹*Department of Physics and State Key Laboratory of Surface Physics, Fudan University, Shanghai 200433, P.R. China*

²*Department of Physics and Institute for Quantum Information and Matter, California Institute of Technology, Pasadena, California 91125, USA*

³*Department of Physics, Massachusetts Institute of Technology, Cambridge, MA 02139, USA*

⁴*Shanghai Branch, Hefei National Laboratory, Shanghai 201315, P.R. China*
(Dated: April 10, 2024)

We explore numerically the intricate interplay between Berry phases in both real and momentum spaces within itinerant magnets. This interplay manifests as an emergent spin-orbit coupling, where charge carriers occupying a Berry-curved band generate an orbital magnetization, inducing a pseudo-magnetic field originating in chiral spin textures. Using density-matrix-renormalization-group techniques, we demonstrate that switching on a band Berry curvature in a metallic ferromagnetic phase results in chiral magnetic textures. Furthermore, employing a two-leg strip geometry, we establish a connection between charge and spin chirality, further supporting this emergent spin-orbit interaction.

The Berry phase[1], a geometric phase accumulated by a quantum state during adiabatic evolution along a closed loop in parameter space, profoundly affects the behavior of electrons in quantum materials. It can originate in either momentum \mathbf{k} -space or real \mathbf{r} -space. In \mathbf{k} -space, the Berry phase can induce chiral motion of electrons, leading to various phenomena such as anomalous Hall conductivity [2], orbital magnetizations (OM)[3, 4], and topological insulators[5, 6]. In \mathbf{r} -space, the Berry phase can be detected by carriers moving through non-coplanar magnetic textures, resulting in observable signatures like Hall conductivity[7–10].

An intriguing scenario arises when both types of Berry phase coexist within a system, enabling carriers to simultaneously perceive \mathbf{r} -space and \mathbf{k} -space Berry phases. This situation is potentially realized in recently discovered ferromagnetism (FM) in graphene systems[11–16]. These systems serve as a realistic platform that encompasses both components: they host Dirac bands, featuring a significant \mathbf{k} -space Berry curvature[15]. Concurrently, FM offers the potential to develop a non-coplanar spin texture, giving rise to the real-space Berry phase.

Recent theoretical studies offer promising insights into this issue, particularly those referenced in[17, 18], which examined the behavior of electrons in itinerant ferromagnets with band Berry curvature. These works reveal that the orbital motion of carriers gives rise to an emergent spin-orbit interaction (SOI), formulated as follows:

$$\begin{aligned} \mathcal{H}_{SOI} &= -(\mathcal{M}_+ - \mathcal{M}_-) B, \\ B &= \frac{\phi_0}{4\pi} \mathbf{S} \cdot (\partial_x \mathbf{S} \times \partial_y \mathbf{S}), \quad \phi_0 = \frac{hc}{e} \end{aligned} \quad (1)$$

where \mathbf{S} represents a spatial-dependent unit vector field indicating the direction of spin polarization in ferromagnets, \mathcal{M}_+ and \mathcal{M}_- denote the orbital magnetization of the majority and minority spin carriers. Distinct from the conventional microscopic SOI, this emergent SOI re-

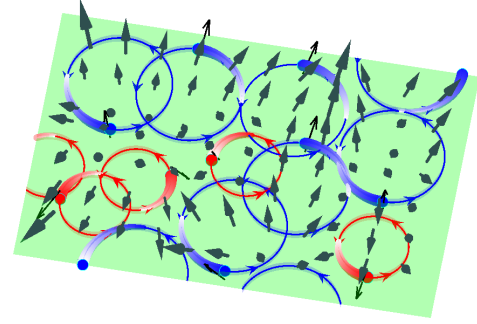


FIG. 1. A cartoon illustrating the spin chirality driven by the emergent SOI. Blue and red balls represent the majority-spin and minority-spin carriers, respectively. The circular trajectories depict their chiral motion due to the band's Berry curvature. The size of the trajectories represents the orbital magnetization of two types of carriers \mathcal{M}_+ and \mathcal{M}_- , which are unequal. It gives rise to the emergent SOI (see Eq.1), leading to a textured mean-field spin polarization, indicated by the black arrows.

spects the SU(2) spin rotation symmetry. Consequently, it modifies the typical collinear spin order observed in itinerant ferromagnets, transforming it into a noncoplanar spin texture with a nonvanishing chirality, as depicted in Fig. 1.

In this paper, we propose a novel mechanism for generating chiral spin textures, distinct from those previously proposed in Refs.[19–22]. These previous studies rely on the nesting of Fermi surfaces to form triple-Q magnetic orders. In contrast, our system requires neither specific nested wave vectors nor a magnetic coupling between itinerant electrons and local magnetic moments. Instead, the spin chirality we have discovered arises from the FM instability of the itinerant electrons and is driven by the OM. In particular, we provide numerical evidence supporting the existence of this interaction as well as its effects. Namely, we employ a minimal

microscopic lattice model that sustains itinerant FM and band with Berry curvature. Using the density-matrix-renormalization-group (DMRG)[23] approach, we investigate the ground state of this model and observe that the itinerant electrons exhibit chiral magnetic order. Moreover, we show that the spin chirality can be switched on and off upon switching the orbital magnetization. This further verifies that the observed spin chirality originates from the emergent SOI proposed in Ref.[17].

Model Hamiltonian and Methodology.— To start, we look for a model that can capture the physics of SOI, i.e., this model needs to introduce magnetic flux to obtain non-zero OM while also incorporating strong Coulomb interaction, leading to Stoner FM instability. The minimal model takes the following form:

$$\begin{aligned} \mathcal{H} = & -t_1 \sum_{\langle jm \rangle, \sigma} \left(e^{i\phi\delta_1^{jm}} c_{j\sigma}^\dagger c_{m\sigma} + H.c. \right) \\ & -t_2 \sum_{\langle\langle jm \rangle\rangle, \sigma} \left(\delta_2^{jm} c_{j\sigma}^\dagger c_{m\sigma} + H.c. \right) \\ & + U \sum_j n_{j\uparrow} n_{j\downarrow} \end{aligned} \quad (2)$$

where $c_{j\sigma}^\dagger$ and $c_{j\sigma}$ are the creation and annihilation operators of an electron with spin $\sigma = \uparrow, \downarrow$ at site j , respectively. The operators $n_{j\uparrow} (n_{j\downarrow})$ count the number of particles with spin \uparrow (\downarrow) at site j . The parameter U denotes the on-site Coulomb interaction strength. Here, $\langle \dots \rangle, \langle\langle \dots \rangle\rangle$ represent the nearest-neighbor(NN) and next-nearest-neighbor(NNN) pairs of sites. And the quantities t_1 and t_2 are the magnitudes of NN and NNN hoppings, respectively. For the NN hopping amplitude between site j and m , we assign $\delta_1^{jm} = +(-)$ depending on whether the electron hops in the direction (reverse direction) of solid black arrow depicted in Fig. 2(a). As for the NNN hopping, δ_2^{jm} takes a value of $+1$ when NNN bond jm aligns with the blue lines in Fig.2(a), and -1 when it aligns with the red lines. The staggered NNN hopping is necessary to break the mirror symmetries along the x and y direction, otherwise, the orbital magnetization would be suppressed due to symmetry constraint.

This model has previously been investigated in Ref.[24, 25], where the case of $\phi = \pi/4$ at a quarter filling was specifically examined, and the ground state exhibited FM behavior. In the FM phase in this model, we expect an emergent SOI, which might lead to a chiral texture. However, none of the aforementioned papers studying this model have shown any evidence of emergent SOI in this FM phase. Therefore, below we show that a new phase with nonzero spin chirality occurs next to this FM phase, in agreement with the prediction of the theory of emergent SOI.

The emergence and disappearance of OM can be intuitively comprehended through a symmetry analysis.

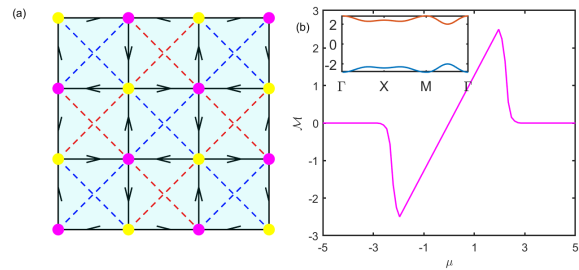


FIG. 2. (a) Schematic of staggered flux square lattice Hubbard model, arrows on NN bond mark the direction of positive phase hopping, blue(red) NNN bond correspond $+(-)t_2$ hopping amplitude. (b) Total OM of one certain spin electron as a function of the chemical potential μ at $t_2/t_1 = 0.6, \phi = \pi/4$. Along the high symmetry points $\Gamma(0,0) - X(\pi,0) - M(\pi,\pi) - \Gamma(0,0)$ in the first Brillouin Zone, the corresponding band structure of the single particle Hamiltonian is presented with the inset. Each band is spin degenerate.

In the most general case where $t_2 \neq 0$, at $\phi = \pi$, the total flux threading through each triangular plaquette amounts to 2π , mirroring the situation at $\phi = 0$. Conversely, at $\phi = \pi/2$, the model breaks mirror symmetry along the direction of the NN-bond but still preserves mirror symmetry along NNN direction and time-reversal symmetry. This occurs because electrons perceive a flux of π in each triangular plaquette. A flux of π per plaquette respects both time-reversal and mirror symmetry along the NNN-bond direction, as both operations transform the flux to $-\pi$ -flux, which is equivalent to π -flux since a flux difference of 2π in each plaquette can be absorbed by a gauge transformation. Since the OM is odd under the time-reversal and mirror operations, it vanishes at these symmetric points of $\phi = 0, \pi/2, \pi$. In contrast, the system with additional symmetry-breaking parameters can give rise to non-zero OM.

Given the pivotal role of OM in governing electron behavior in our system, we present some specific calculations for the single-particle Hamiltonian[26]. These calculations are based on the semi-classical wave packet formalism of Bloch electrons, as outlined in Ref. [27]. Fig. 2(b) depicts the OM as a function of the Fermi level μ , considering the specific parameter of $t_2/t_1 = 0.6, \phi = \pi/4$ where both time-reversal and mirror symmetry are broken. As the carrier density increases, the absolute value of \mathcal{M} rises and attains its peak when the Fermi level intersects the valence band. When μ sits within the band gap, the OM exhibits a linear variation with μ , and the slope of this line corresponds to the Chern number of the occupied bands.

Based on the topological band characterized by Berry curvature, which underlies the OM discussed previously, we now introduce Coulomb interaction U to induce Stoner FM instability. However, itinerant FM is not commonly observed in Hubbard models. Therefore, we

choose some special parameters to obtain well-established FM states. These include the flat-band FM[28], which exhibits a divergent density of states, and Nagaoka FM[29], applicable to infinite U Hubbard models with a single hole on the half-filled background. By manipulating the phase factor ϕ attached to electrons hopping or the filling factor in these FM metallic states, we expect that itinerant electrons will exhibit non-zero spin chirality in the presence of a large OM. This chirality could potentially enable the electrons to gain additional energy, thereby overcoming the energy cost associated with spin stiffness[17].

Flat band FM to chiral metallic phase.— First, we focus on the nearly flat band limit by fine-tuning parameters with $t_2/t_1 = 0.6, \phi = \pi/4$. At this point, a finite Coulomb interaction of $U = 4.0$ is required to maintain a ferromagnetic metallic state[24]. At the dilute limit, the spin structure factor $S_{\mathbf{k}} = \frac{1}{N_s} \sum_{\langle i,j \rangle} \langle \mathbf{S}_i \cdot \mathbf{S}_j \rangle e^{i\mathbf{k} \cdot (\mathbf{r}_i - \mathbf{r}_j)}$ depicted in Fig.3(a) suggests that the system is not ferromagnetic. Furthermore, Fig.3(b) reveals that within this parameter range, the inverse charge compressibility remains relatively small, indicating that the system behaves as a paramagnetic metal (PM).

According to the concept of orbital magnetization inducing spin chirality, the system undergoes a transition from a fully spin-polarized state to a chiral metallic (CM) phase, as depicted with green solid circles in Fig.3(a). This transition occurs because OM increases as more charge carriers are loaded into the band. In the chiral metallic phase, the spin chirality measured on each triangular plaquette is present in the inset of Fig.3(b). This result is measured at a filling factor of $\nu = 13/30$ (labeled with arrow) which means there are 52 electrons on 6×10 sites, where each site has two spin states \uparrow and \downarrow . Besides, in Fig.3(b), we show the filling dependence for the inverse charge compressibility $\kappa_c^{-1} = \frac{\partial \mu}{\partial n}$. We can observe that within the range of $\nu < 0.43$, the inverse compressibility remains a small value. This implies that the system is a compressible metal. As we approach half-filling, the inverse compressibility exhibits a peak, indicating that the system is an insulator at half-filling in the thermodynamic limit. From the evolution of the spin structure factor at high-symmetry points shown in Fig.3(a), we find that within the range of $0.13 < \nu < 0.26$, the structure factor at the (0,0) point is dominant. This is consistent with the characteristics of FM states. As the filling number increases, the structure factor at the center point of the first Brillouin zone sharply decreases, while the structure factor at other high-symmetry points gradually increases. In the chiral metal region, the dominant component is the (π, π) component.

We would like to emphasize that several related numerical studies[30, 31] on the Hofstadter-Hubbard model have claimed the existence of skyrmion or spin textured metals on the high magnetic field limit. This oc-

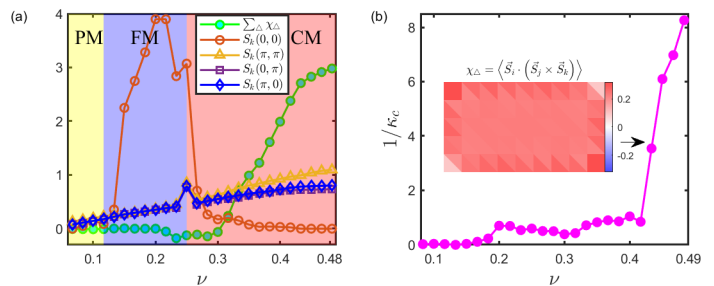


FIG. 3. (a) Total spin chirality $\sum_{\Delta} \chi_{\Delta}$ and static spin structure factor $S_{\mathbf{k}}(k_x, k_y)$ on high-symmetry points of multi-leg ladders (both open boundary condition (OBC) in x, y direction) with $N_x = 10, N_y = 6$ as a function of filling factor ν , (b) Inverse charge compressibility $\kappa_c^{-1} \approx \frac{N_e^2}{N_s} [E(N_e + \delta N_e) + E(N_e - \delta N_e) - 2E(N_e)] / \delta N_e^2$ (where $E(N_e)$ is the ground-state energy with N_e electrons on $N_s = N_x \times N_y$ sites and $\delta N_e^2 = 2^2$) with different filling factor ν , there is a discontinuity when approaching the half-filling case. The inset shows the pattern of discrete spin chirality $\langle \mathbf{S}_i \cdot (\mathbf{S}_j \times \mathbf{S}_k) \rangle$ in the ground state. This result was measured under the parameters indicated by the black arrow in (b). Here, ijk are chosen such that the loop $i \rightarrow j \rightarrow k \rightarrow i$ winds in the clockwise direction.

urrence arises from the competition between the exchange interaction and the Hofstadter band. As the correlated electrons are subjected to a uniform magnetic field in these models, these spin textures still align with the conventional understanding of quantum Hall ferromagnets.[32, 33]. However, a crucial distinction in our system lies in the fact that conduction electrons encounter a staggered flux with zero net flux. As a result, the chiral spin textures we have discovered can be interpreted as skyrmion without the constraint of Landau levels.

Chiral metallic phase based on Nagaoka FM.— Without loss of generality, we turn our attention to another well-established Nagaoka FM state which doesn't require fine-tuning t_2/t_1 . Hence we can exclude the impact of the flat band while remaining within the FM region when tuning phase factor ϕ . In the limit of $U \rightarrow \infty$, the interaction term in \mathcal{H} is replaced by a nonlocal constraint of no double occupancy at each site, i.e. $n_j = 0, 1$. As we approach the half-filling, a fully polarized FM state emerges at $\phi = 0, \pi/2, \pi$, and then we obtain a chiral metallic phase when away from these points (see Fig.4(a)). Additionally, this chiral spin-textured phase remains metallic, as evidenced by the power-law decay of single-particle Green's function $|\langle c_{0\sigma}^\dagger c_{r\sigma} \rangle|$ (red-circle line in Fig.4(b,c)). And it exhibits strong magnetic order as observed in Fig.4(b,c) (blue-triangular line). The parameter $K_s < 2$ suggests the divergent susceptibility in 2D limit.

The flux can be used as a knob to control the OM sensitively. In order to provide further confirmation that spin chirality indeed originates from the emergent spin-orbital

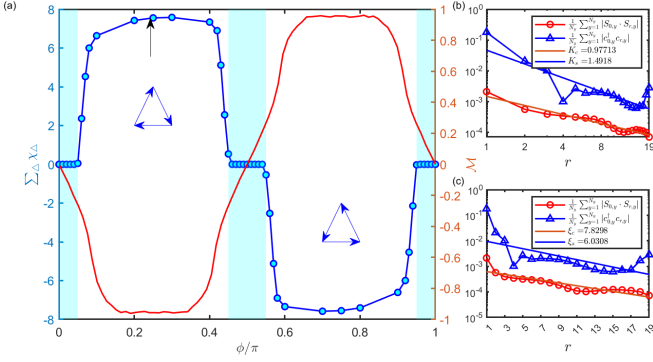


FIG. 4. (a) At the filling factor of $\nu = 19/40$ (two holes away from half-filling), $t_2/t_1 = 0.2, U = \infty$, the total spin chirality (blue-dotted line) of the $N_x = 10, N_y = 4$ open cluster is plotted as a function of the phase factor ϕ . The green shadow region represents the zero-spin chirality region. The corresponding total OM \mathcal{M} (red-line) of the non-interacting system at $\mu = -1$ is also shown. In this case, the lower band is nearly fully occupied, while the upper band is empty. (b) Log-log plot of single-particle Green's function $\langle \langle c_{0\sigma}^\dagger c_{r\sigma} \rangle \rangle$ (mark as a blue-triangular), and spin-spin correlation $|\langle \mathbf{S}_0 \cdot \mathbf{S}_r \rangle|$ (mark as a red-circle) as a function of distance r (r is the column index). The power exponent K_c, K_s are obtained by fitting $r^{-K_c(K_s)}$. (c) Same data but in semilogarithmic scale. The exponential fit $\propto e^{-r/\xi}$ yields the corresponding correlation length ξ_c, ξ_s as shown with the legend. These results are calculated on $N_x \times N_y = 20 \times 4$ system (Both OBC in x and y direction.) and correspond to the parameter indicated by the black arrow in (a).

interaction, we manipulate the total flux penetrating a plaquette. As seen in Fig.4(a), the chirality (depicted by the blue-dotted line) vanishes at the time-reversal-symmetric or mirror-symmetric points of $\phi = 0, \pi/2, \pi$. Furthermore, the spin chirality is reversed resulting from reversing the orbital part to get the opposite OM when switching the ϕ in the range of $(0, \pi/2)$ to $\phi \in (\pi/2, \pi)$ as shown by the red line in Fig.4(a). This outcome underscores the role of the $-MB$ interaction in transferring the time reversal of orbital motion to the spin degree of freedom.

As we scan the flux ϕ , we observe a regime at $\phi = N\pi/2$ (where N is any integer) in which the spin chirality disappears entirely. This observation agrees with the prediction made in Ref. [17]. Specifically, at $\phi = N\pi/2$, the model regains mirror symmetry, as discussed in our prior symmetry analysis, leading to a suppression of orbital magnetization near these points (illustrated by the red curve in Fig. 4(a)). Therefore, one also expects the suppression of the spin chirality since spin chirality occurs only if the magnetization \mathcal{M} surpasses a finite threshold so that the energy gain from the emergent SOI overcomes the energy cost due to spin stiffness. In addition, we find a broader plateau of zero-spin chirality region on cylindrical geometry where the boundary condition at $y = 0$ is

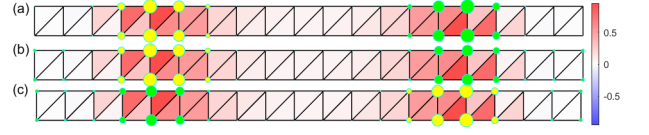


FIG. 5. The spin chirality $\langle \mathbf{S}_i \cdot (\mathbf{S}_j \times \mathbf{S}_k) \rangle$ measured on 2×20 system at $U = \infty, t_2/t_1 = 0.2$, the electron number is set as $N_e = 38$. (a) green and yellow circles respectively denote the + and - sign of spin polarization $\langle S_i^z \rangle = \langle n_i^\uparrow - n_i^\downarrow \rangle$. The electron number density of (b) spin-up $\delta n_i^\uparrow = \langle n_i^\uparrow - \nu \rangle$ and (c) spin-down $\delta n_i^\downarrow = \langle n_i^\downarrow - \nu \rangle$ after subtracting the mean value, with yellow circles corresponding to positive values and green to negative values.

set to be periodic (see Supplement [34]). This is because when enclosing the boundary along y -direction introduce a “frustration” that constrains the solid angle spanned by spin texture. Such frustration favors collinear FM and constrains the chiral order [35].

Nevertheless, the spin texture is not directly observable in experiments. Therefore, we aim to identify realistic signatures linking to the chiral spin-textured metal. The graphene system exhibits itinerant FM and OM, making it an ideal candidate for studying these phenomena. Notably, the energy scale of spin-orbit coupling in graphene is negligible. Hence, the detection of spin chirality in these systems cannot be explained by conventional wisdom but instead is driven by the emergent spin-orbit coupling that we have proposed. Subsequently, we will briefly discuss some unique experimental features inherent to our chiral spin textures underlying graphene systems.

As the charge carriers with the majority or minority spin process opposite Berry phases and sense opposite magnetic fields, the energies of majority-spin and minority-spin carriers are shifted downward and upward by the emergent SOI, respectively. Namely, the amount of the energies shift between spin-majority and spin-minority carriers at the Fermi level is given by $\delta E_\sigma(k) = \sigma B m_\sigma(k)$. Consequently, this results in a spatial modulation of spin polarization that mirrors the pattern of spin chirality,

$$\delta n_\sigma(\mathbf{r}) = \sigma B(\mathbf{r}) \oint_{k_F^\sigma} \frac{m_\sigma(\mathbf{k}) d\mathbf{k}}{(2\pi)^2 v_F^\sigma(\mathbf{k})} \quad (3)$$

where the integration of \mathbf{k} is along the Fermi surface. Indices $\sigma = +, -$ represent the carriers of majority and minority spin, respectively. $v_F^\sigma(\mathbf{k})$ and $m_\sigma(\mathbf{k})$ refer to the magnitude of Fermi velocity and the self-rotation orbital magnetic moment at momentum \mathbf{k} , respectively.

Here, in our DMRG results, we can measure the quantity of $\langle S_i^z \rangle$. From Fig.5, we indeed observe the spin polarization $\langle S_i^z \rangle$ and charge density δn_i^σ are both modulated in the same way as the spin chirality. In reality, We expect the local spin polarization $\langle \mathbf{S} \rangle$ to form a chiral

pattern with a nonvanishing $\langle \mathbf{S} \rangle \cdot (\partial_x \langle \mathbf{S} \rangle \times \partial_y \langle \mathbf{S} \rangle)$. This type of magnetic texture can be probed through nano-SQUID measurement[36, 37]. Notably, for the case of a fully spin-polarized phase, $n_\downarrow = 0$, Eq.(3) predicts a spatially modulated spin polarization and a spatially modulated charge density. This will be directly detectable through STM[38–40]

In summary, by conducting a general symmetry analysis of a minimal model, we can break symmetry by manipulating the model parameters, thus highlighting the impact of the Berry phase. Numerical studies of its ground state indicate that itinerant ferromagnets with band Berry phase can naturally form chiral spin textures. Further evidence suggests that the spin chirality is driven by emergent spin-orbit interaction. These findings align with the theoretical predictions outlined in Ref.[17].

Given this numerical evidence, which focuses on the spin chirality within the FM state, it would be beneficial to detect spontaneous spin chirality in the graphene system through transport experiments and high-resolution magnetic imaging. Besides, this phenomenon inspires us to explore more physical consequences of the interplay between real-space and momentum-space Berry phase on correlated electronic states.

We thank Leonid Levitov, Ting-Kuo Lee and Zhihuan Dong for their fruitful suggestions. This work is supported by the National Key Research and Development Program of China Grant No. 2022YFA1404204, and the National Natural Science Foundation of China Grant No. 12274086.

* yanchen99@fudan.edu.cn

- [1] M. V. Berry, Quantal phase factors accompanying adiabatic changes, *Proceedings of the Royal Society of London. A. Mathematical and Physical Sciences* **392**, 45 (1984).
- [2] N. Nagaosa, J. Sinova, S. Onoda, A. H. MacDonald, and N. P. Ong, Anomalous hall effect, *Rev. Mod. Phys.* **82**, 1539 (2010).
- [3] D. Xiao, M.-C. Chang, and Q. Niu, Berry phase effects on electronic properties, *Rev. Mod. Phys.* **82**, 1959 (2010).
- [4] T. Thonhauser, D. Ceresoli, D. Vanderbilt, and R. Resta, Orbital magnetization in periodic insulators, *Phys. Rev. Lett.* **95**, 137205 (2005).
- [5] X.-L. Qi and S.-C. Zhang, Topological insulators and superconductors, *Rev. Mod. Phys.* **83**, 1057 (2011).
- [6] M. Z. Hasan and C. L. Kane, Colloquium: Topological insulators, *Rev. Mod. Phys.* **82**, 3045 (2010).
- [7] K. Ohgushi, S. Murakami, and N. Nagaosa, Spin anisotropy and quantum hall effect in the kagomé lattice: Chiral spin state based on a ferromagnet, *Phys. Rev. B* **62**, R6065 (2000).
- [8] R. Shindou and N. Nagaosa, Orbital ferromagnetism and anomalous hall effect in antiferromagnets on the distorted fcc lattice, *Phys. Rev. Lett.* **87**, 116801 (2001).
- [9] N. Nagaosa and Y. Tokura, Emergent electromagnetism in solids, *Physica Scripta* **2012**, 014020 (2012).
- [10] T. Fujita, M. B. A. Jalil, S. G. Tan, and S. Murakami, Gauge fields in spintronics, *Journal of Applied Physics* **110**, 121301 (2011).
- [11] Y. Cao, V. Fatemi, A. Demir, S. Fang, S. L. Tomarken, J. Y. Luo, J. D. Sanchez-Yamagishi, K. Watanabe, T. Taniguchi, E. Kaxiras, et al., Correlated insulator behaviour at half-filling in magic-angle graphene superlattices, *Nature* **556**, 80 (2018).
- [12] Y. Cao, V. Fatemi, S. Fang, K. Watanabe, T. Taniguchi, E. Kaxiras, and P. Jarillo-Herrero, Unconventional superconductivity in magic-angle graphene superlattices, *Nature* **556**, 43 (2018).
- [13] H. Zhou, T. Xie, A. Ghazaryan, T. Holder, J. R. Ehrets, E. M. Spanton, T. Taniguchi, K. Watanabe, E. Berg, M. Serbyn, et al., Half-and quarter-metals in rhombohedral trilayer graphene, *Nature* **598**, 429 (2021).
- [14] U. Zondiner, A. Rozen, D. Rodan-Legrain, Y. Cao, R. Queiroz, T. Taniguchi, K. Watanabe, Y. Oreg, F. von Oppen, A. Stern, et al., Cascade of phase transitions and dirac revivals in magic-angle graphene, *Nature* **582**, 203 (2020).
- [15] E. Y. Andrei and A. H. MacDonald, Graphene bilayers with a twist, *Nature materials* **19**, 1265 (2020).
- [16] A. M. Seiler, F. R. Geisenhof, F. Winterer, K. Watanabe, T. Taniguchi, T. Xu, F. Zhang, and R. T. Weitz, Quantum cascade of correlated phases in trigonally warped bilayer graphene, *Nature* **608**, 298 (2022).
- [17] Z. Dong and L. Levitov, Chiral stoner magnetism in dirac bands (2022), arXiv:2208.02051 [cond-mat.mes-hall].
- [18] Z. Dong, O. Ogunnaike, and L. Levitov, Collective excitations in chiral stoner magnets, *Phys. Rev. Lett.* **130**, 206701 (2023).
- [19] I. Martin and C. D. Batista, Itinerant electron-driven chiral magnetic ordering and spontaneous quantum hall effect in triangular lattice models, *Phys. Rev. Lett.* **101**, 156402 (2008).
- [20] D. Solenov, D. Mozyrsky, and I. Martin, Chirality waves in two-dimensional magnets, *Phys. Rev. Lett.* **108**, 096403 (2012).
- [21] R. Ozawa, S. Hayami, and Y. Motome, Zero-field skyrmions with a high topological number in itinerant magnets, *Phys. Rev. Lett.* **118**, 147205 (2017).
- [22] J. W. F. Venderbos, M. Daghofer, J. van den Brink, and S. Kumar, Switchable quantum anomalous hall state in a strongly frustrated lattice magnet, *Phys. Rev. Lett.* **109**, 166405 (2012).
- [23] M. Fishman, S. R. White, and E. M. Stoudenmire, The ITensor Software Library for Tensor Network Calculations, *SciPost Phys. Codebases*, 4 (2022).
- [24] X.-F. Su, Z.-L. Gu, Z.-Y. Dong, S.-L. Yu, and J.-X. Li, Ferromagnetism and spin excitations in topological hubbard models with a flat band, *Phys. Rev. B* **99**, 014407 (2019).
- [25] R. L. Doretto and M. O. Goerbig, Flat-band ferromagnetism and spin waves in topological hubbard models, *Phys. Rev. B* **92**, 245124 (2015).
- [26] Specific calculation processes and detailed results on orbital magnetization are presented in the supplementary materials.
- [27] D. Xiao, Y. Yao, Z. Fang, and Q. Niu, Berry-phase effect in anomalous thermoelectric transport, *Phys. Rev. Lett.* **97**, 026603 (2006).
- [28] H. Tasaki, Extension of nagaoka’s theorem on the large-u

- hubbard model, Phys. Rev. B **40**, 9192 (1989).
- [29] Y. Nagaoka, Ferromagnetism in a narrow, almost half-filled s band, Phys. Rev. **147**, 392 (1966).
- [30] F. A. Palm, M. Kurttutan, A. Bohrdt, U. Schollwöck, and F. Grusdt, Ferromagnetism and skyrmions in the hofstadter–fermi–hubbard model, New Journal of Physics **25**, 023021 (2023).
- [31] J. K. Ding, L. Yang, W. O. Wang, Z. Zhu, C. Peng, P. Mai, E. W. Huang, B. Moritz, P. W. Phillips, B. E. Feldman, and T. P. Devereaux, Particle-hole asymmetric ferromagnetism and spin textures in the triangular hubbard-hofstadter model (2023), arXiv:2309.07876 [cond-mat.str-el].
- [32] S. L. Sondhi, A. Karlhede, S. A. Kivelson, and E. H. Rezayi, Skyrmions and the crossover from the integer to fractional quantum hall effect at small zeeman energies, Phys. Rev. B **47**, 16419 (1993).
- [33] A. H. MacDonald, H. A. Fertig, and L. Brey, Skyrmions without sigma models in quantum hall ferromagnets, Phys. Rev. Lett. **76**, 2153 (1996).
- [34] See more results on cylinder geometry, marked with “ y -PBC”.
- [35] A simple way to see it is by considering the extreme limit of a two-leg ladder, where introducing PBC directly enforces the chirality in two nearby plaquettes along the y direction to cancel each other out.
- [36] C. L. Tschirhart, M. Serlin, H. Polshyn, A. Shragai, Z. Xia, J. Zhu, Y. Zhang, K. Watanabe, T. Taniguchi, M. E. Huber, and A. F. Young, Imaging orbital ferromagnetism in a moiré chern insulator, Science **372**, 1323 (2021), <https://www.science.org/doi/pdf/10.1126/science.abd3190>.
- [37] C. Tschirhart, E. Redekop, L. Li, T. Li, S. Jiang, T. Arp, O. Sheekey, T. Taniguchi, K. Watanabe, M. Huber, et al., Intrinsic spin hall torque in a moiré chern magnet, Nature Physics , 1 (2023).
- [38] Y. Choi, H. Kim, Y. Peng, A. Thomson, C. Lewandowski, R. Polski, Y. Zhang, H. S. Arora, K. Watanabe, T. Taniguchi, J. Alicea, and S. Nadj-Perge, Tracing out correlated chern insulators in magic angle twisted bilayer graphene (2020), arXiv:2008.11746 [cond-mat.str-el].
- [39] X. Liu, G. Farahi, C.-L. Chiu, Z. Papic, K. Watanabe, T. Taniguchi, M. P. Zaletel, and A. Yazdani, Visualizing broken symmetry and topological defects in a quantum hall ferromagnet, Science **375**, 321 (2022), <https://www.science.org/doi/pdf/10.1126/science.abm3770>.
- [40] K. P. Nuckolls, R. L. Lee, M. Oh, D. Wong, T. Soejima, J. P. Hong, D. Călugăru, J. Herzog-Arbeitman, B. A. Bernevig, K. Watanabe, T. Taniguchi, N. Regnault, M. P. Zaletel, and A. Yazdani, Quantum textures of the many-body wavefunctions in magic-angle graphene, Nature **620**, 525–532 (2023).
- [41] M.-C. Chang and Q. Niu, Berry phase, hyperorbits, and the hofstadter spectrum: Semiclassical dynamics in magnetic bloch bands, Phys. Rev. B **53**, 7010 (1996).
- [42] Z. Wang and P. Zhang, Orbital magnetization and its effects in spin-chiral ferromagnetic kagomé lattice, Phys. Rev. B **76**, 064406 (2007).
- [43] Z. Wang, P. Zhang, and J. Shi, Orbital magnetization and its effect in antiferromagnets on the distorted fcc lattice, Phys. Rev. B **76**, 094406 (2007).
- [44] D. Ceresoli, T. Thonhauser, D. Vanderbilt, and R. Resta, Orbital magnetization in crystalline solids: Multi-band insulators, chern insulators, and metals, Phys. Rev. B **74**, 024408 (2006).
- [45] L. Liu, H. Yao, E. Berg, S. R. White, and S. A. Kivelson, Phases of the infinite u hubbard model on square lattices, Phys. Rev. Lett. **108**, 126406 (2012).

Supplemental Material for “Chiral Spin Textures Driven by Emergent Spin-Orbit Interaction: A Numerical Study”

This supplementary material contains the process and results of calculating the orbital magnetization of single-particle Hamiltonian, as well as more results of DMRG numerical calculations, including parameter settings for convergence, measurements of the ground state under several characteristic parameters, and results on the cylindrical geometry (compare with the results on open cluster).

Appendix Section I: Band structures and orbital magnetization for the single particle model

To investigate the orbital magnetization properties of the model, we invoke a well-known formula based on the semi-classical wave packet paradigm for Bloch electrons[41] as shown in the following.

$$\begin{aligned} \mathcal{M}(\mu) &= \sum_n \int^{\mu} \frac{d\mathbf{k}}{(2\pi)^2} [m_n(\mathbf{k}) + \frac{e}{\hbar} \Omega_n(\mathbf{k}) [\mu - \varepsilon_n(\mathbf{k})]] \\ &= \mathcal{M}_c + \mathcal{M}_\Omega \end{aligned} \quad (\text{S1})$$

Here $\varepsilon_n(\mathbf{k})$ is the band structure for the non-interacting part of this model. The term $m_n(\mathbf{k})$ in Eq(S1) represents the orbital magnetic moment generated by self-rotation of electron wave packets at momentum \mathbf{k} , taking the form of $m_n(\mathbf{k}) = -\frac{ie}{2\hbar} \langle \nabla_{\mathbf{k}} u_n(\mathbf{k}) | \times [H(\mathbf{k}) - \varepsilon_n(\mathbf{k})] | \nabla_{\mathbf{k}} u_n(\mathbf{k}) \rangle$, in which $H(\mathbf{k})$ is the crystal Hamiltonian. The Berry curvature $\Omega_n(\mathbf{k}) = i \langle \nabla_{\mathbf{k}} u_n(\mathbf{k}) | \times | \nabla_{\mathbf{k}} u_n(\mathbf{k}) \rangle$, also contributes to the orbital magnetization due to the center-of-mass motion of electron wave packets. The integration runs over states with energies below the Fermi energy μ , the first part in Eq(S1) is the conventional part \mathcal{M}_c arising from self-rotation of electron wave packet and the second part \mathcal{M}_Ω accounts for the contribution from the chiral edge state of a topological band.

But directly calculating $\Omega_n(\mathbf{k})$ and $m_n(\mathbf{k})$ for this model is complicated. Therefore, we first insert a complete base $1 = \sum_{n'} |u_{n'}\rangle \langle u_{n'}|$ and rewrite the formula as follows:

$$\begin{aligned} \Omega_n(\mathbf{k}) &= i \sum_{n' \neq n} \left\langle \frac{\partial u_n}{\partial k_x} | u_{n'} \right\rangle \left\langle u_{n'} | \frac{\partial u_n}{\partial k_y} \right\rangle - c.c \\ m_n(\mathbf{k}) &= \frac{ie}{\hbar} \sum_{n' \neq n} \left\langle \frac{\partial u_n}{\partial k_x} | H - \varepsilon_n | u_{n'} \right\rangle \left\langle u_{n'} | \frac{\partial u_n}{\partial k_y} \right\rangle - c.c \end{aligned} \quad (\text{S2})$$

Further with the Identity as:

$$\left\langle u_{n'} | \frac{\partial}{\partial \mathbf{k}} | u_n \right\rangle = \frac{\left\langle u_{n'} | \frac{\partial H(\mathbf{k})}{\partial \mathbf{k}} | u_n \right\rangle}{\varepsilon_{n'} - \varepsilon_n} \quad (\text{S3})$$

The Berry curvature and the orbital magnetic moment carried by the Bloch electron can be rewritten in the following form:

$$\begin{aligned} \Omega_n(\mathbf{k}) &= i \sum_{n' \neq n} \frac{\left\langle u_n | \frac{\partial H}{\partial k_x} | u_{n'} \right\rangle \left\langle u_{n'} | \frac{\partial H}{\partial k_y} | u_n \right\rangle}{(\varepsilon_{n'} - \varepsilon_n)^2} - c.c. \\ m_n(\mathbf{k}) &= i \frac{e}{\hbar} \sum_{n' \neq n} \frac{\left\langle u_n | \frac{\partial H}{\partial k_x} | u_{n'} \right\rangle \left\langle u_{n'} | \frac{\partial H}{\partial k_y} | u_n \right\rangle}{\varepsilon_{n'} - \varepsilon_n} - c.c. \end{aligned} \quad (\text{S4})$$

which is more tractable for numerical calculation.

The FigS1 below shows the band dispersion relationship $\varepsilon_n(\mathbf{k})$ ((a),(d)), Berry curvature $\Omega_n(\mathbf{k})$ ((b),(e)), and orbital magnetic moment $m_n(\mathbf{k})$ ((c),(f)) information distributed along highly symmetric points under three different characteristic parameters. At $\phi = 0, \pi/2, \pi$, Berry curvature and orbital magnetic moment are both equal to zero, due to the symmetry of the time reversal and the space inversion. At $\phi = \pi/4$, the non-zero t_2 causes the system to open the gap at $X(\pi, 0)$, and at the same time breaks the symmetry of time reversal and space inversion, thus obtaining the non-vanishing Berry curvature and orbital magnetic moment.

The FigS2 below illustrates the two components of the total orbital magnetization calculated in the main text. It can be seen that the OM from these two parts are always opposite, reflecting the opposite circulation motion of the two components. All these results are consistent with the previous articles[4, 42–44].

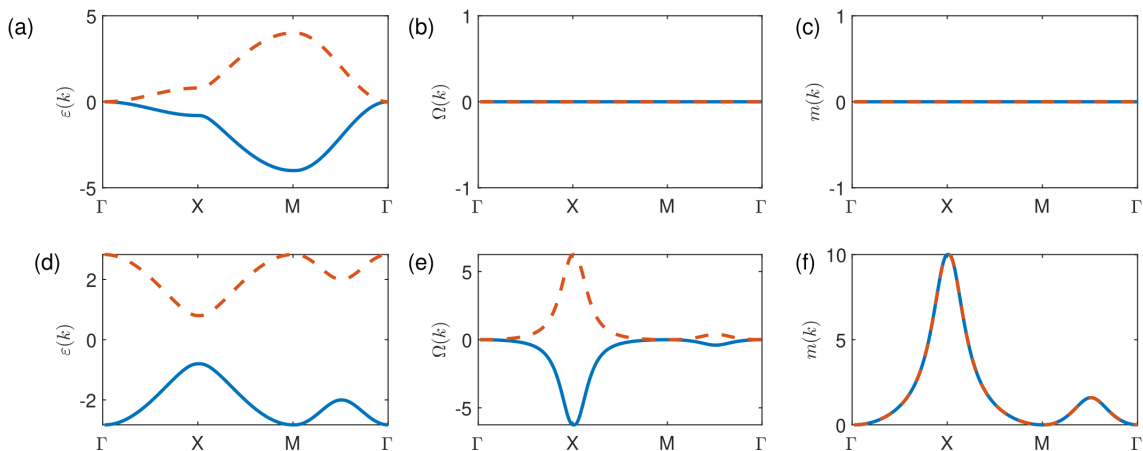


FIG. S1. At $\phi = \pi/4$, the band structure of the tight binding model at (a) $t_2/t_1 = 0.0$, and (d) $t_2/t_1 = 0.2$. The Berry curvature $\Omega_n(\mathbf{k})$ of (b) $t_2/t_1 = 0.0$, and (e) $t_2/t_1 = 0.2$. The orbital magnetic moment $m_n(\mathbf{k})$ of (c) $t_2/t_1 = 0.0$, and (f) $t_2/t_1 = 0.2$

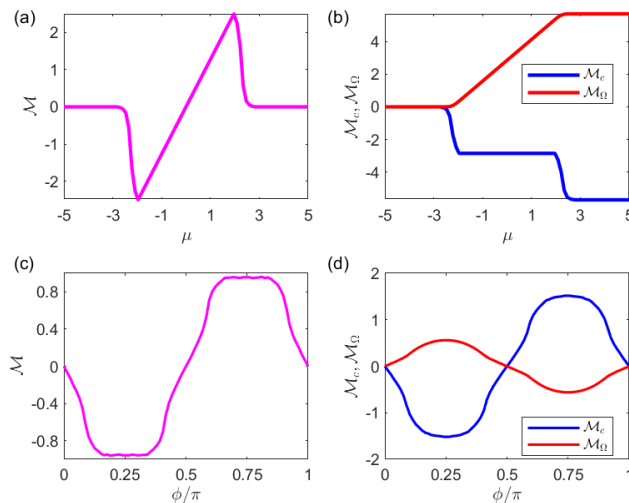


FIG. S2. Orbital magnetization of the non-interacting model as a function of (a) chemical potential μ and (c) phase factor ϕ . (b) Its two components \mathcal{M}_c (blue line) and \mathcal{M}_Ω (red line) as a function of electron chemical potential μ at $t_2/t_1 = 0.6$, $\phi = \pi/4$. (d) \mathcal{M}_c (blue line) and \mathcal{M}_Ω (red line) as a function of phase factor ϕ at $t_2/t_1 = 0.2$, $\mu = -1$.

Appendix Section II: Additional numerical simulation information

II. A. Details of the numerical simulation

We perform DMRG calculations[23] for this generalized Hubbard model on multi-leg ladders (both open boundary conditions in x and y directions) and multi-leg cylinders (open boundary condition in x direction and periodic boundary condition in y direction). We mainly compute the properties of 4-leg and 6-leg systems (with sizes up to 4×20 and 6×10 , with corresponding truncation errors $\sim 10^{-6}$). We perform at most 200 sweeps to search for the ground state within the sector of the total S_z component equal to zero and the bond dimension is set up to $D = 8000$ to get converged results. We believe these results are reliable in predicting the behavior of electrons in realistic two-dimensional systems.

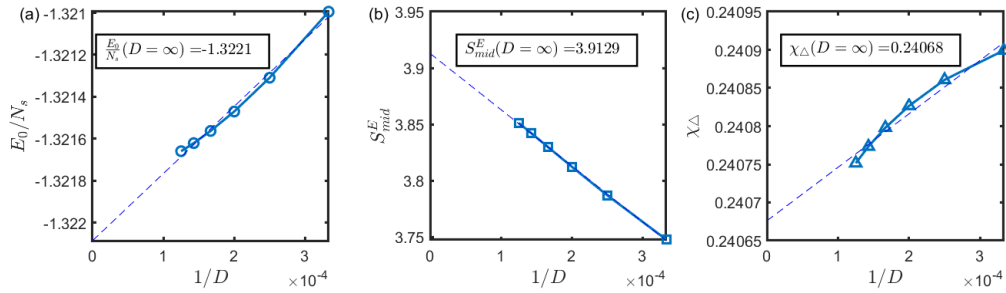


FIG. S3. (a) The ground state energy per site E_0/N_s , (b) Entanglement entropy S_{mid}^E measured at the center of the systems, (c) mean spin chirality χ_Δ as a function of the inverse of bond dimension $1/D$. Using linear extrapolation (as indicated by the dashed line) to obtain the result at $D = \infty$ (marked with a text box in the corresponding graph).

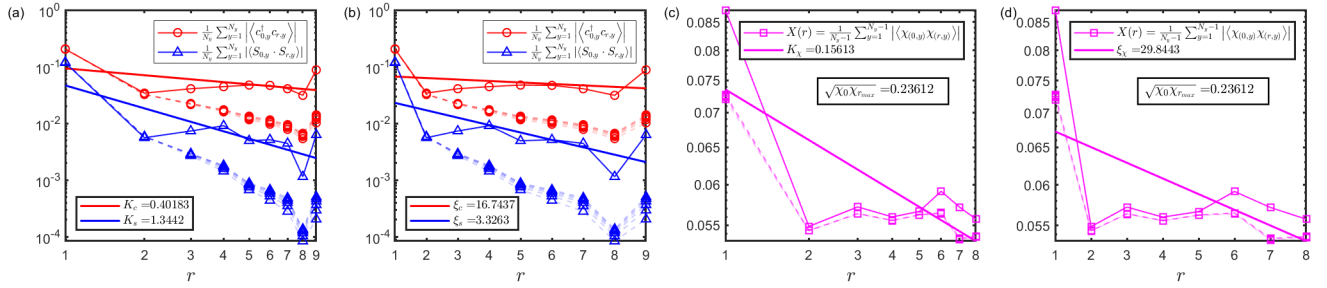


FIG. S4. (a) Log-log plot (b) and Log-linear plot of single-particle Green's function $\left| \left\langle c_{0\sigma}^\dagger c_{r\sigma} \right\rangle \right|$, spin-spin correlation $|\langle \mathbf{S}_0 \cdot \mathbf{S}_r \rangle|$ versus distance, the index r labels the column index. (c) Log-log plot (d) and Log-linear plot of chiral-chiral correlation $|\langle \chi_0 \chi_r \rangle|$ versus r , K_χ, ξ_χ corresponds to the power and correlation length. The dashed line corresponds to the results for different bond dimensions ($D = 3000, 4000, 5000, 6000, 7000, 8000$), the solid line represents the result extrapolated to $D = \infty$, and the straight line shows the results of power-law and exponential fitting applied to the extrapolated results.

II. B. Convergence of the DMRG calculation

In this part, we show the bond dimension dependence of ground state energy per site E_0/N_s (Fig.S3(a)), entanglement entropy S_E (Fig.S3(b)) and mean spin chirality χ_Δ (S3(c)) for the parameter corresponding to the inset of Fig.3(b) in the main text. During the calculation, the bond dimension is set as $D = 3000, 4000, 5000, 6000, 7000, 8000$. For these metallic states, we found that the entanglement entropy is always rapidly increasing, indicating that these states are challenging for DMRG calculations. However, the results for energy and average spin chirality show relatively good convergence.

Additionally, the results below (see Fig.S4) show the single-particle correlation $\left| \left\langle c_{0\sigma}^\dagger c_{r\sigma} \right\rangle \right|$, spin-spin correlation $|\langle \mathbf{S}_0 \cdot \mathbf{S}_r \rangle|$, and chiral-chiral correlation $|\langle \chi_0 \chi_r \rangle|$ for different bond dimensions, further confirming that the ground state is an incompressible metal with spin chirality. The square root of the chiral-chiral correlation at the farthest distance $\sqrt{\chi_0 \chi_{r_{\max}}} \approx 0.23612$ is also close to the average spin chirality $\chi_\Delta(D = \infty) \approx 0.24068$ measured for a single triangle.

II. C. Spin chirality in response to orbital magnetization

In this section, we will present specific data to illustrate the response of spin chirality to orbital magnetization.

Below we show the ground state properties of the system with two characteristic parameters ϕ . When $\phi = \pi/2$, the system is time-reversal invariant and the corresponding orbital magnetization is equal to zero. The structure factor of spin-spin correlation shown in FigS5(a) indicates the ground state is a ferromagnetic metallic state related to the Nagaoka FM theorem. Although this theorem strictly holds only in the case of a single hole, some numerical evidence has confirmed that the Nagaoka FM state can exist in a range close to half-filling in the infinite- U Hubbard model[45].

As the parameter ϕ is set to $\pi/4$, the system obtains orbital magnetization. As a result, FigS5(c) shows that the electrons exhibit spin chirality. At CM region, the dominant component of spin structure factor is located at $M(\pi, \pi)$

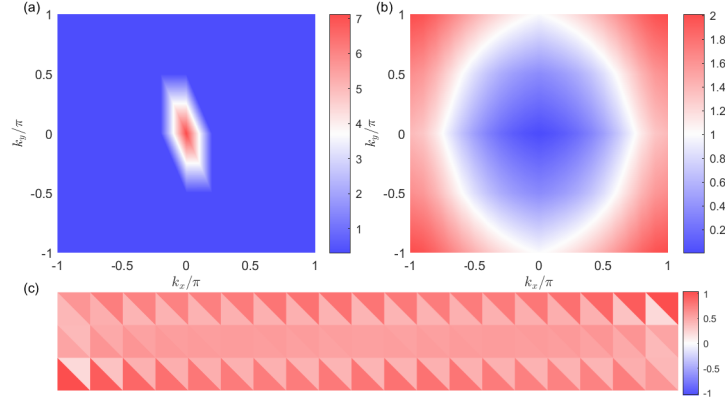


FIG. S5. Measurements of the chiral metallic phase based on Nagaoka FM with $U = \infty, t_2/t_1 = 0.2$. Static spin structure factor at (a) $\phi = 0$ (b) $\phi = 4/\pi$ (c) Spin chirality $\langle \mathbf{S}_i \cdot (\mathbf{S}_j \times \mathbf{S}_k) \rangle$ pattern of the CM ground state.

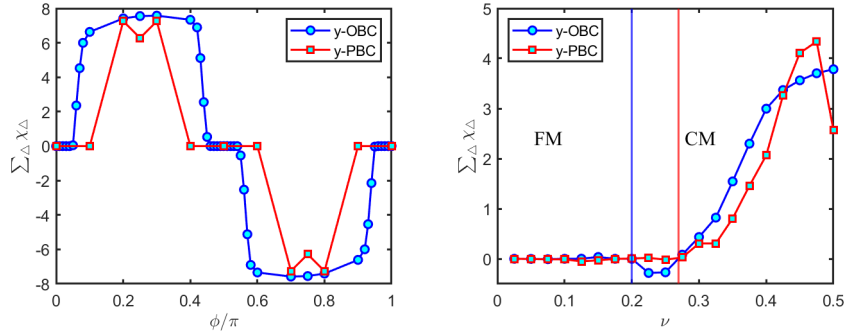


FIG. S6. Total chiral spin order as a function of different (a) ϕ/π with $U = \infty, t_2/t_1 = 0.2$, (b) and filling factor ν with $U = 4, t_2/t_1 = 0.6$ on $N_x \times N_y = 10 \times 4$ open cluster (depicted with blue-circle) and cylinder (depicted with red-square).

momentum point as shown in FigS5(b).

II. D. Results for the y-PBC cylinder geometry

In this part, we present numerical simulation results on cylindrical geometry to further support our argument. The results on the cylinder and the results with open boundary conditions in both x and y directions exhibit similar trends. So the conclusions are roughly consistent. The main difference is the presence of larger zero-spin chiral regions in cylindrical geometry, as we explained in the main text.

From FigS6(b), when adjusting the particle population density, the system with periodic boundary condition in the y direction has a certain lag in entering the chiral metal phase. The same phenomenon is observed when adjusting the phase factor attached to the electron hopping. As illustrated in FigS6(a), the spin chirality is nearly zero when approaching the symmetric points of $\phi = 0, \pi/2, \pi$. Moreover, the results on the cylinder show that there is a larger parameter interval around these symmetric points to keep the system in the ferromagnetic phase.